Facet-dependent Electronic Properties of Silicon Nanowires

by

Xiaodan Xu

B.Sc. (Department of Physics & Astronomy), University Of Waterloo, 2007

B.Sc. (Department of Physics), Harbin Institute of Technology, 2007

A THESIS SUBMITTED IN PARTIAL FULFILLMENT OF

THE REQUIREMENTS FOR THE DEGREE OF

MASTER OF APPLIED SCIENCE

in

The Faculty of Graduate Studies

(Electrical and Computer Engineering)

THE UNIVERSITY OF BRITISH COLUMBIA

(Vancouver)

July, 2009

Abstract

The effects of surface reconstruction and progressive hydroxylation on the electronic properties of [110] hexagonal silicon nanowires are investigated by ab initio calculations within the density functional theory. Progressive hydroxylation changes the density of states close to valence band maxima and leads to a general decrease in the band gap. The magnitude of band gap reduction is dependent on the facet where the hydroxyl group is bonded. While a high reduction in band gap (10%) is observed for hydroxylation on (111) facets, for (001) facets the reduction is more pronounced (21%) only when there is a (3×1) reconstruction. The reduction in band gap is generally accompanied by an off-center radial shift in the location of the charge density arising from the HOMO. These results go to show the impact of surface reconstruction and termination groups on the electronic properties of Si nanowires, which are important for using these materials for biosensor and transistor applications. In order to synthesize Si nanowires, this thesis also explores the self-organization of citrate-stabilized gold nanoparticles onto amino-terminated surfaces. The deposition of citrate-stabilized gold nanoparticles onto hydrogen-terminated Si surface with pH modification is also investigated and is compared with the self-organized method. Both approaches show gold colloid deposition.

Contents

List of Tables

List of Figures

Dedication

I want to dedicate this work to my dear parents and brother.

Statement of Co-Authorship

Chapters 1, 3, and Appendix A were written by the author. Chapter 2 is a published paper, which is co-authored by myself and Dr. Peyman Servati. I performed the simulation and analysis; I generated and prepared the figures; I wrote the first draft of the paper, and participated in the collaborative effort that led to the final version of the paper.

Chapter 1

Introduction

1.1 Semiconductor nanowires

Semiconductor nanowires (NWs) have gained attention recently because of their important properties such as large surface-to-volume ratio, high transport mobility, and tunable band structure. A Si NW can be considered as bulk silicon confined in 1-dimension with chemical passivation on the surface. The properties of semiconductor NWs are always determined by the properties of the semiconductor material of which they are made. Various semiconductor materials, such as silicon, germanium, gallium arsenide, and gallium nitride, which have different electronic and optical properties, may have great potential use in a variety of technological applications. Compared to carbon nanotubes (CNTs), semiconductor NWs represent a more recent development in the field of nanoscale devices and have a substantially greater range of chemical properties leading to more practical applications and methods of organization. Particularly, Si and Ge-based NW devices are much more desirable for electronic and other applications because of their compatibility with existing Si CMOS integrated-circuit technology.

Controlled growth of NWs in predetermined configurations would be beneficial to device fabrication. Recent progress in NW synthesis will be briefly reviewed in the following section. Also, the molecular structure of SiNWs studied experimentally by other researchers will also be discussed.

1.1.1 Nanowire synthesis

Synthesis of semiconductor NWs has made a strong impact on nanotechnology. Various methods have been used to realize 1D nanostructures. The most widely used technique is vapor-liquid-solid (VLS) [1] growth which has been successful in producing silicon nanowires (SiNWs) and germanium nanowires (GeNWs) in large quantities. Despite over 40 years of study, many aspects of VLS growth are not well understood. Since 1997, new techniques such as laser-assisted chemical vapor deposition (CVD) [2], oxide-assisted CVD [3], metal-catalyzed molecular beam epitaxy (MBE) [4], and chemical beam epitaxy (CBE) [5] have been developed. However, how to fabricate desired 1D semiconductor nanostructures with well-controlled atomic structures is still a challenging issue.

SiNW growth using metal (Au is widely used) clusters as a solvent (catalyst) can be explained by the corresponding Metal-Si phase diagram. Generally, with increasing amount of Si vapor condensation and dissolution, Si and Au form an alloy and liquefy. The volume of the alloy droplet increases and the elemental contrast decreases. As the concentration of Si increases in the alloy droplet, nucleation of the NW begins. Once the Si nanocrystal nucleates at the liquid-solid interface, crystallization at the interface starts to form NWs. For a steady VLS growth process, NW growth species in the liquid droplet should remain in balance, *i.e.* the number of atoms transferred from the vapor phase to the droplet per unit time is equal to that transformed from liquid to the crystal phase.

An advantage of VLS is that patterned deposition of catalyst particles yields patterned nanowires. Also, it provides an efficient approach to obtain uniformed-sized NWs since the diameter of the NWs is determined by the diameter of the catalyst particles. Yang *et al.* have shown that precise diameter control of NWs is only limited by the size distribution of the seed particles [6].

Patterned gold catalyst can be formed by evaporation, metal deposition, photolithography, or nanocluster formation [7–10]. Gold thin film, however, does not provide good diameter control due to the randomness of the film breakup at reaction temperatures, and the use of photolithography to define the location of the catalyst is relatively expensive. The colloidal nanoparticle (NP) methods are particularly suitable for assembly and growth of nanomaterials because of their controlled sizes, shapes, compositions and surface functionalities

of synthesized NPs [11]. An aqueous colloidal solution of Au NPs is usually prepared by the reduction of $HAuCl_4$ with sodium citrate [12]. The immobilization of the colloidal Au NPs on a silicon substrate can then be achieved by the specific electrostatic interaction of charged gold NPs with the amine functions of an amino-terminated monolayer on the modified Si surface. The amino-terminated monolayer renders the substrates positively charged and allows for the deposition of the negatively charged gold colloids efficiently. Yang *et al.* have demonstrated that an appropriate colloidal solution could be used to grow vertically aligned, monodispersed SiNW arrays by the conventional VLS-CVD approach [6]. And by varying the concentration of the colloidal solution, the seeding density on the substrate surface can also be controlled. The deposition of gold colloidal NPs was studied in this work and the results will be discussed in Appendix A.

Chidsey and co-workers developed a linker-free approach to deposit citrate-stabilized gold colloids onto oxide-free Si substrates by acidifying the gold colloid solution with HF or HCl, which prevents oxide formation and allows for epitaxial growth of NWs [13]. Figure 1.1 (a) shows scanning electron microscope (SEM) images from the GeNW array. Vertically aligned GeNWs of controlled diameter and uniform length were grown by this linker-free approach followed by a two-step temperature process [14, 15] without the need of high temperature to promote epitaxial growth. Epitaxial growth of vertical NWs is one pathway to obtain an organized and aligned array of NWs. As indicated in Figure 1.1 (c), the growth temperature was far below 400 °C, which is very promising for "post-integration" of NW devices. Researchers [14, 15] concluded that high temperature is required for the formation of a high-quality GeNW/Ge interface which is necessary for initiation of epitaxial NW growth. However, high temperature is not required for the subsequent NW growth. Furthermore, NW tapering can be avoided by using this growth procedure.

Successful synthesis of high density and purity of uniform single crystalline GeNWs via simple thermal evaporation of Ge powder has been reported by several research groups [16–18]. Yu *et al.* [16] developed a two-furnace thermal evaporation system where the NW growth temperature and source evaporation temperature were separately controlled, as illustrated in Figure 1.2. Large quantities of single crystalline GeNWs were synthesized, and a high yield of straight NWs with relatively good diameter uniformity was obtained in the temperature range between 450 and 600 °C. Compared to other methods such as CVD

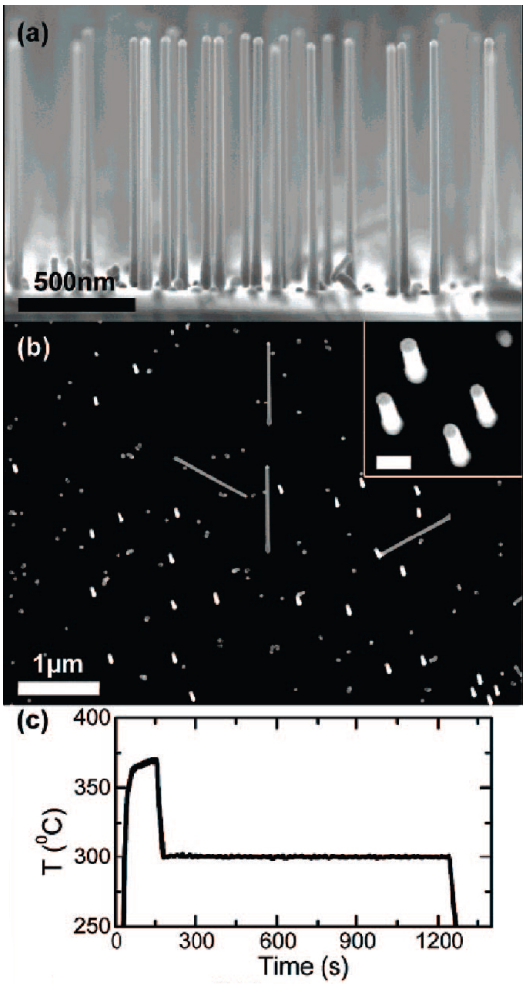

Figure 1.1: (a) Cross-section SEM of GeNWs grown epitaxially on Si(111) substrates from 40 nm gold colloids deposited using the HF-addition method, showing predominantly vertically oriented Ge nanowires of uniform diameter and length, (b) plan-view SEM of the sample in (a) showing the other three ⟨111⟩ growth directions and (inset) magnified view of vertical Ge nanowires (scale bar is 100 nm), (c) two-step temperature profile used to grow the GeNWs in (a) and (b). Reprinted with permission from [13]. Copyright 2007 American Chemical Society.

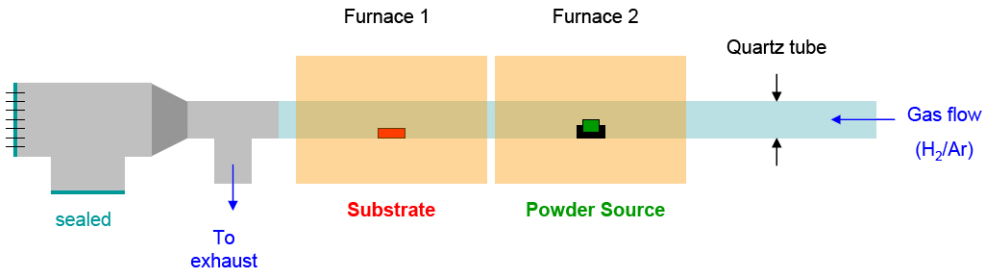

Figure 1.2: Thermal evaporation GeNW synthesis system.

and laser ablation, the simple thermal evaporation of powder source uses a much simpler reaction setup and nonhazardous materials and gases such as SiH_4 and GeH_4. The furnace system we are building for NW growth is quite similar to this.

1.1.2 Nanowire structure

For the VLS growth, due to the presence of a Au catalyst at the tip of the NWs, the interface and surface energies play important roles for the nucleation and growth direction of different sizes of NWs. Lieber *et al.* [10] have found that by using silane (SiH_4) as a vapor-phase reactant, SiNWs with small diameters between 3 and 10 nm prefer to grow along the $\langle 110 \rangle$ direction. This is consistent with the result reported by other researchers [19, 20]. However, a very recent report by the same research group showed contrasting results [21] using different reactant source Si_2H_6, where millimeter-long SiNWs with diameters of 20-80 nm grow preferentially along the $\langle 110 \rangle$ direction independent of diameter. It was speculated to be caused by the higher catalytic decomposition rate of Si_2H_6 leading to a faster growth rate. Schmidt *et al.* proposed a model based on the liquid-solid interfacial energy and the Si surface energy [19]. It is believed that NW growth is driven by the minimum state of the total system energy of the NW. Because the surface to volume ratio is high and the bulk crystal energy is independent of NW orientation, only surface and interface energies need to be considered. NWs preferentially grow in the direction minimizing their total interface and surface energy. High-resolution transmission electron microscopy (HRTEM) images confirmed that the $\{111\}$ interfaces have the lowest liquid-solid interfacial energy [10, 20].

The resulting side facets are the energetically most favorable surfaces with low surface energies.

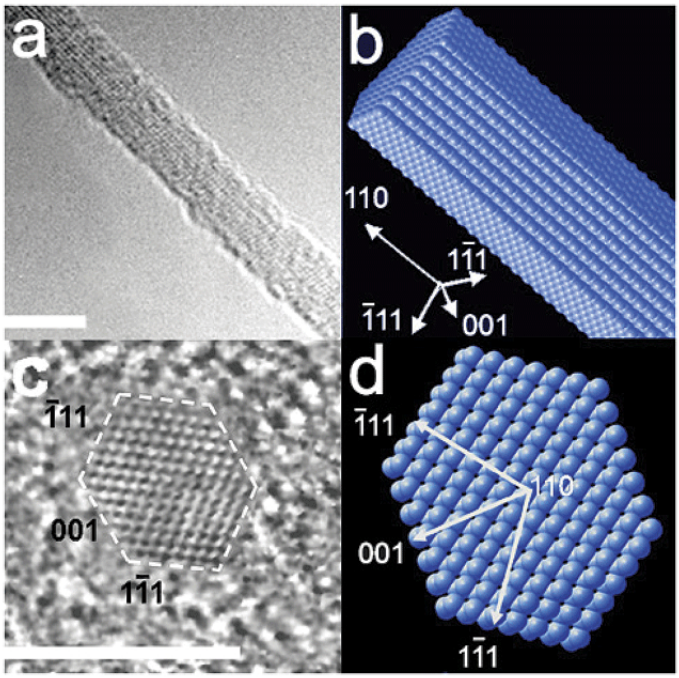

Figure 1.3: (a) TEM images of 3.8-nm SiNWs grown along the 110 direction, (c) HRTEM cross-sectional image, and equilibrium shapes for the (b) NW and the (d) NW cross sections predicted by Wulff construction. The scale bars are 5 nm. SiNWs dispersed in epoxy were sectioned with a microtome to slices ca. 50 nm thick and were then transferred to copper TEM grids. Reprinted with permission from [10]. Copyright 2004 American Chemical Society.

Figure 1.3 shows HRTEM studies of a SiNW that grows along the $\langle 110 \rangle$ direction [10]. The cross-sectional image reveals that the NW has a hexagonal cross section with well-developed facets corresponding to the low-free-energy (111) and (100) planes. The molecular-scale SiNW model built in Chapter 2 of this thesis is based on this experimental analysis. A similar faceted structure (Figure 1.4) of small-diameter SiNWs after HF-treatment has also been studied by scanning tunneling microscopy (STM) by Lee *et al.* [22]. They found that the Si(001) surface is terminated by the symmetric dihydride (SiH_2) and the Si-H

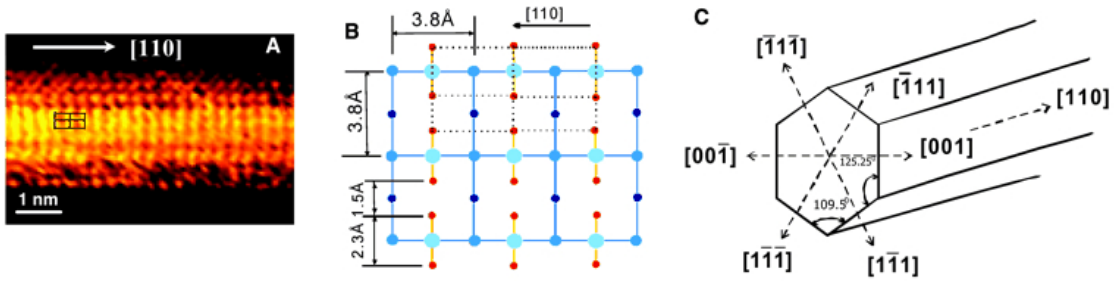

Figure 1.4: STM image and schematic view of a SiNW with a Si (001) facet. Crystallographic directions are shown. (A) Constant-current STM image of a SiNW on a HOPG substrate. The wire's axis is along the [110] direction. (B) Schematic view of the dihydride phase on Si (001). Red and large blue circles represent H and Si atoms in the dihydride phase, respectively. Small blue circles correspond to Si atoms on the layers below. (C) Schematic view of a Si nanowire bounded by four (111)-type facets and two (001)-type facets. The wire's axis is along the [110] direction. From [22]. Reprinted with permission from AAAS.

bonds are oriented perpendicularly to the NW axis. To our knowledge, this is the only experimental report on the bonding structure of a NW surface. However, in bulk silicon, the H-saturated Si(001) surface usually undergoes a 2 $\times$ 1 reconstruction. It was also observed that the saturated surface could consist of a 3 $\times$ 1 phase which involved repeated alternating monohydride and dihydride units [23].

Hydroxyl groups play an important role in many technologically relevant processes. The formation of hydroxyls on the Si surface can be important for preparing an ideal surface for atomic layer deposition of metal oxide dielectrics, based on the ligand exchange reaction. Also, the presence of surface hydroxyls enables the patterning of a multifunctional organic molecule thus avoiding the possibility of multiple adsorption geometries. This is of particular interest in surface modification for biosensing applications [24]. Partial hydroxylation of the clean Si(001) surface can be achieved by simply direct exposure to water [25], while complete hydroxylation of the clean Si(001) surface is not firmly established yet [26].

The surface morphology of NWs combined with their crystalline structures influences the NW-device performance as a result of its effect on the electronic properties, which will be addressed in chapter 2 in detail [27].

1.2 Surface passivation effect on NW-based devices

Nano-devices based on NW structures have recently attracted much attention because NWs provide great flexibility in their electronic properties. For example, NWs with different electrical properties can be produced through choosing appropriate semiconductor materials [28, 29]. It has been shown that SiNWs can be successfully doped by adding reaction precursors of boron (B) or phosphorus (P) to the vapor source to modify the electrical properties [30]; the characteristic p-type or n-type behavior was observed. Other types of electrical characteristics of NWs can be achieved by their surface modification. The high surface areas of NWs suggest that surface effects could play dominant roles in determining their physical properties. It was observed that the electrical properties of NW devices could be affected by various surface species including molecules adsorbed from the environment [7, 31].

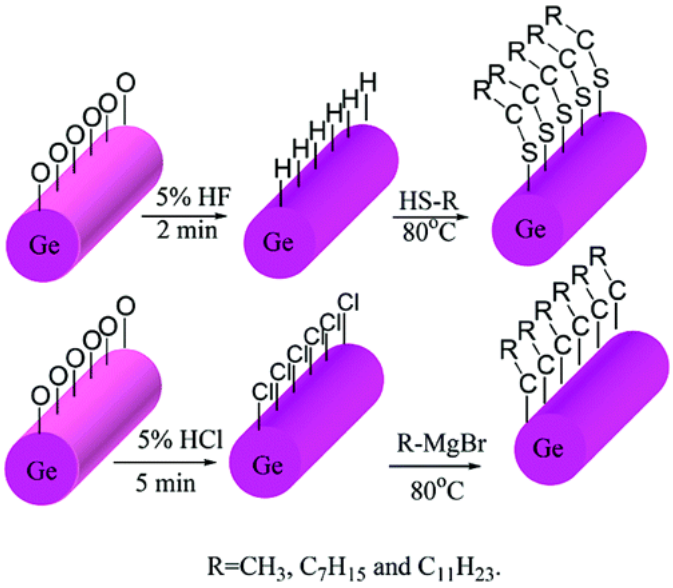

Figure 1.5: GeNW functionalization schemes using alkanethiols (top) and Grignard reactions (bottom). Reprinted with permission from [33]. Copyright 2005 American Chemical Society.

The first stage of surface effect is oxidation. In order to develop effective surface passivation strategies of NWs, the underlying oxidation process must be understood. Silicon, the most important material in the semiconductor industry, its oxide SiO_2 is chemically and electronically stable and its surface can be chemically passivated with a variety of organic species. However, the surface chemistry of Ge is much more complicated due to the water solubility of GeO_2 and the lack of a stable oxide. Hence, it is critical for GeNWs to develop robust chemical passivation methods against oxidation. Much effort has been made recently to study the surface chemistry of as-grown and air-exposed GeNWs. Dai *et al.* have employed long chain alkylthiol and Grignard reactions [32] to investigate GeNW functionalization, as depicted in Figure 1.5 [33]. Native oxide removal and H- (alkylthiol reactions) or Cl- (Grignard reactions) passivation can be achieved with diluted HF or HCl treatment. Different strategies for chemically modifying the NW surfaces, such as wet and dry oxidation, sulfidation, organic monolayer and in situ thiol passivations, were also explored by other researchers [31]. The nanostructure surfaces were characterized using surface techniques, such as X-ray photoelectron spectroscopy (XPS) and also high-resolution electron microscopy imaging (Figure 1.6). The NWs studied in [31] also exhibited the $\langle 110 \rangle$ growth orientation and were characterized by $\{111\}$ and $\{100\}$ faceted surfaces, as recently experimentally verified by cross-sectional HRTEM which was discussed above [10, 22].

Field effect transistors (FETs) made from doped NWs have been demonstrated [7, 34]. Cui *et al.* have reported that NW FETs after surface modification showed increases by an order of magnitude in both the transconductance and mobility compared to conventional metal oxide FETs [7], which suggests that many of the electrical properties of the NW-based devices are determined by the large number of surface states.

In addition, NWs also have great potential as elements for sensor applications [24, 36]. NW-based sensors exhibit exceptional sensitivity due to the great impact of surface effects on the electrical properties, whereas surface modfication makes possible manipulations with their selectivity. For example, Huang *et al.* have found that the performance of poly-Si NWs can be significantly boosted by the water passivation effect [35], which makes the material attractive for sensing because of its low cost and compatibility with various substrates. Figure 1.7 (a) shows the SEM picture of a NW device. The authors believed that, in wet environment (DI water), the abundant H^+ and/or OH^- may diffuse into the grain

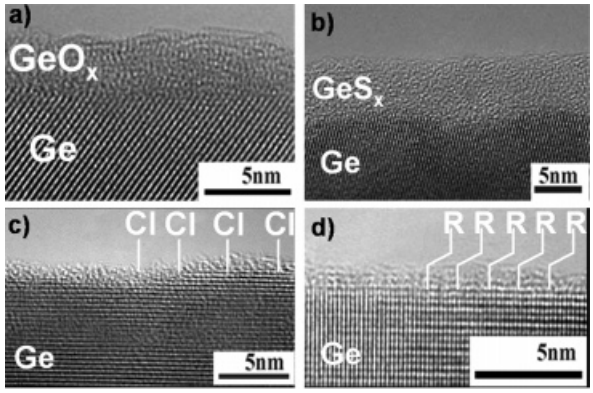

Figure 1.6: High-resolution TEM images of (a) untreated Ge nanowire surface showing the nonuniform oxide and carbonaceous contamination coating and Ge nanowires with (b) sulfide coating, (c) chloride termination, and (d) covalently bonded hexyl monolayer termination. Reprinted with permission from [31]. Copyright 2004 American Chemical Society.

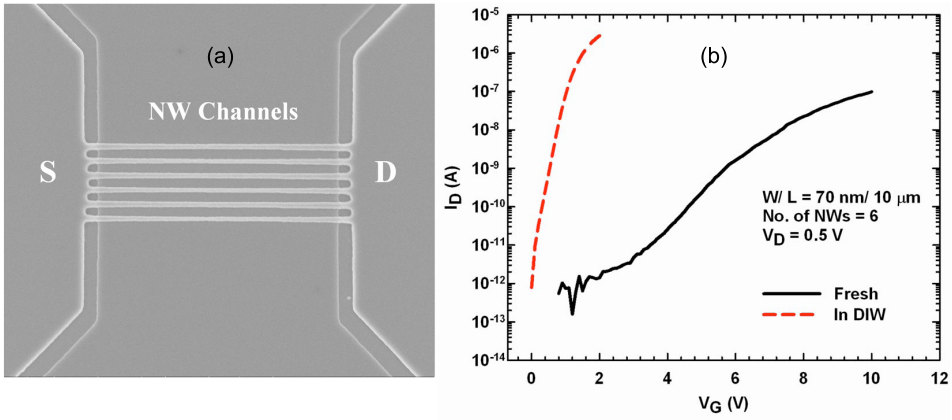

Figure 1.7: (a) SEM images of a device which contains six NW channels. Planar width and thickness of each NW is 70 nm and 90 nm, respectively; (b) Transfer characteristics of a device operating in dry and wet (DI water, denoted as DIW) environments. Reprinted with permission from [35]. Copyright 2007, American Institute of Physics.

boundaries and terminate on the dangling bonds resulting in a dramatic improvement of device performance (Figure 1.7 (b)). For the purpose of biological detection [36], the poly-Si NW's surface is modified, as illustrated in Figure 1.8. To some extent, the transduction mechanism in NW biosensors is similar to the operation of NW FETs. The change of electrical signal of the NW FET may reflect the amount of molecules of interest immobilized on the NW surface.

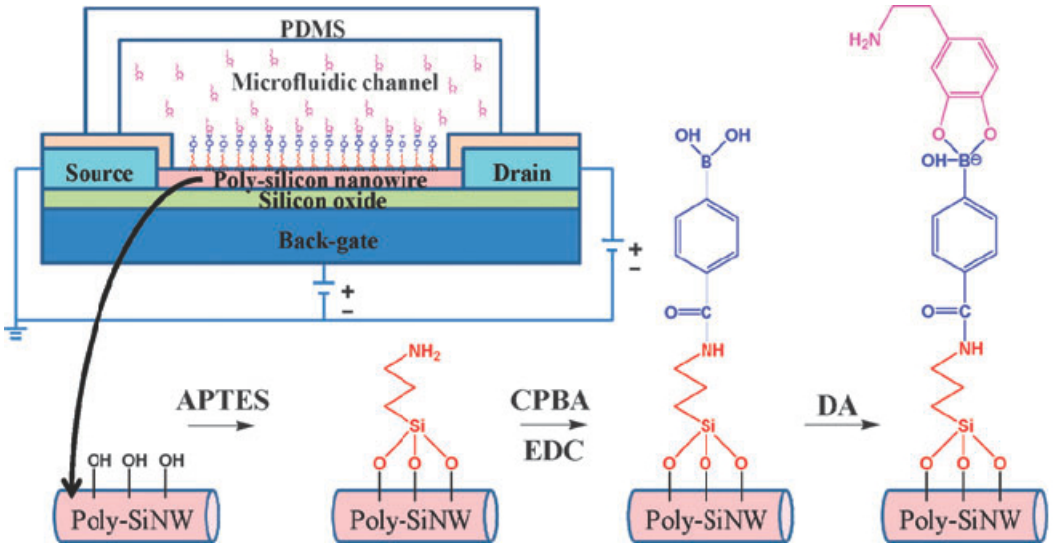

Figure 1.8: Functionalization of poly-SiNW for dopamine detection by poly-SiNW FET. Schematic illustration of poly-SiNW surface modification is shown [36].

NW-based photovoltaic devices have also been investigated recently [37, 38]. SiNW solar cells of p-type/intrinsic/n-type (p-i-n) coaxial structure were successfully fabricated by Lieber and co-workers [37]. The authors suggested that in NW solar cells applications, passivating the NW surface and grain boundaries could significantly reduce recombination process hence improve the NW photovoltaic performance [39]. The role of surface states in the electronic properties of NWs needs to be investigated in much greater detail.

Surface modification could potentially allow for engineering of electronic properties such as band gap and carrier mobilities. However, experiments on surface modification of semiconductor NWs are less abundant. For device applications such as NW FETs and sensors, the NW surface properties must be understood and controlled. Thus, detailed investigation of

the surface chemistry of NWs and exploration of various chemical passivation pathways is valuable for understanding and controlling the behaviour of devices.

1.3 Electronic structure calculations of silicon nanowires

In bulk silicon, the fundamental band gap is indirect, and the conduction band minima are sixfold degenerate, where they are located along the ⟨100⟩ directions near the X point (usually referred to as Δ minima). The effective transport mass both of electrons and holes is a direct consequence of the band structure. Compared with bulk material, nanowires may show different electronic and optical properties due to the strong quantum confinement effect in the lateral dimensions. Other than the reduced dimension, surface morphology (passivation and surface reconstruction) as mentioned in the previous sections is also expected to have strong impact on NW's properties and consequently to affect the device characteristics. Hence it is desirable to study the electronic properties, e.g. effective mass, band gaps and band edges.

We have chosen density functional theory (DFT) rather than other ab initio methods such as Hartree-Fock (HF), configuration-interaction, many-body perturbation and coupled-cluster theory because they provide better accuracy and reasonable computation time for systems such as SiNWs with a large number of atoms. DFT is an established alternative for solving the Schrödinger equation and includes important electron correlation effects that are neglected by the HF theory. To our knowledge, most of the recent theoretical calculations of the electronic properties of nanowires have been performed by ab initio DFT [40, 41], including works that have reliably predicted the change in band gap as a function of nanowire diameter.

Our calculations were carried out with the SIESTA package [42]. The parameters used in calculations are mentioned in chapter 2. The SIESTA method is a fully self-consistent implementation of DFT, based on a flexible linear combination of atomic orbitals (LCAO) basis set and pseudopotential approach, with Order-N scaling. The pseudopotentials are standard norm-conserving [43, 44], treated in the fully non-local form [45]. The exchange

and correlation potential is treated within Kohn-Sham DFT. Both the local density approximation (LDA) [46] and the generalized gradients approximation (GGA) [47] are available in SIESTA. Systems are treated in a supercell scheme which uses three lattice vectors to describe the periodicity. Strictly confined basis orbitals, which go to zero beyond a certain radius from their center, are used to achieve sparsity of the Hamiltonian and overlap matrices. Once the electronic problem is solved, the total energy of the system can be obtained, as well as the forces on the atoms and the stress tensor. This allows one to perform structural relaxations and molecular dynamics simulations. In addition, a wide range of properties such as the electronic band structure and partial density of states can be readily obtained.

Despite the popularity of DFT within either GGA or LDA, the calculated band gaps of SiNWs are usually underestimated. It was shown that the energy band gap can be corrected by using the many-body perturbation method based on the GW approximation [48], where the self-energy can be approximated to a product of the Green's function, G, and the dynamical screened interaction, W. However, the convergence of GW calculations can be very slow [49]. Because the GW corrections are mainly dependent on NW diameters [50], the energy gap corrections are not likely to differ significantly when the NW surfaces are modified. Nevertheless, the general character of band strucutre of bulk silicon was reproduced, and DFT calculations are expected to predict the correct trend of the change in band gap and gap edge energies due to surface modifications.

1.4 Thesis overview

The second chapter [27], which is a published journal paper in Nano Letters, is a theoretical study of the electronic properties of SiNWs. In this thesis, we used the SIESTA package [42] to perform ab initio calculations within the density functional theory. This work investigates the impact of hydroxylation on different facets of silicon nanowire on the electronic properties such as band gap, effective mass, and density of states. The surface reconstruction on Si(001) facets is also considered. Using a infinitely long NW model with hexagonal cross section based on previous reported experimental data, various Si-hydroxyl

environments have been examined. We show that the chemistry of surface termination can change the internal electronic structure of SiNWs.

Appendix A of this thesis will discuss some preliminary experimental results for gold NPs deposition on silicon wafer by two different approaches. The gold NPs are the catalysts for nanowire growth and define the diameter and site of NWs. The morphology of the deposition was studied by Atomic Force Microscopy (AFM) and Auger Emission Spectroscopy (AES) analysis.

Bibliography

[1] Wanger, R. S.; Ellis, W. C. *Appl. Phys. Lett.* **1964**, *4*, 89.

[2] Morales, A. M.; Lieber, C. M. *Science* **1998**, *279*, 208.

[3] Wang, N.; Zhang, Y. F.; Tang, Y. H.; Lee, C. S.; Lee, S. T. *Appl. Phys. Lett.* **1998**, *73*, 3902.

[4] Wu, Z. H.; Mei, X. Y.; Kim, D.; Blumin, M.; Ruda, H. E. *Appl. Phys. Lett.* **2002**, *81*, 5177.

[5] Bjork, M. T.; Ohlsson, B. J.; Sass, T.; Persson, A. I.; Thelander, C.; Magnusson, M. H.; Deppert, K.; Wallenberg, L. R.; Samuelson, L.; *Appl. Phys. Lett.* **2002**, *80*, 1058.

[6] Hochbaum, A. I., Fan, R.; He, R.; Yang, P. *Nano Lett.* **2005**, *5*, 457.

[7] Cui, Y.; Zhong, Z; Wang, D; Wang, W. U.; Lieber, C. M. *Nano Lett.* **2003**, *3*, 149.

[8] Jin, S.; Whang, D. M.; McAlpine, M. C.; Friedman, R. S.; Wu, Y.; Lieber, C. M. *Nano Lett.* **2004**, *4*, 915.

[9] Zheng, G. F.; Lu, W.; Jin, S.; Lieber, C. M. *Adv. Mater.* **2004**, *16*, 1890.

[10] Wu, Y.; Cui, Y.; Huynh, L.; Barrelet, C. J.; Bell, D. C.; Lieber, C. M. *Nano Lett.* **2004**, *4*, 433.

[11] *Colloids and colloid assemblies : synthesis, modification, organization, and utilization of colloid particles*; Caruso, F., Ed.; Wiley-VCH: Weinheim, Germany, 2004.

[12] Frens, G. *Nature Phys. Sci.* **1973**, *241*, 20.

[13] Woodruff, J. H.; Ratchford, J. B.; Goldthorpe, I. A.; McIntyre, P. C.; Chidsey, C. E. D. *Nano Lett.* **2007**, *7*, 1637.

[14] Adhikari, H.; Marshall, A. F.; Chidsey, C. E. D.; and, McIntyre, P. C. *Nano Lett.* **2006**, *6*, 318.

[15] Greytak, A. B.; Lauhon, L. J.; Gudiksen, M. S.; Lieber, C. M. *Appl. Phys. Lett.* **2004**, *84*, 4176.

[16] Yu, B. X.; Sun, X. H.; Calebotta, G. A.; Dholakia, G. R.; Meyyappan, M. *J. Clust. Sci.* **2006**, *17*, 579.

[17] Sun, X. H.; Didychuk, C.; Sham, T. K.; Wong, N. B. *Nanotechnology* **2006**, *17*, 2925.

[18] Sutter, E.; Ozturk, B.; Sutter, P. *Nanotechnology* **2008**, *19*, 435607.

[19] Schmidt, V.; Senz, S.; Gosele, U. *Nano Lett.* **2005**, *5*, 931.

[20] Cai, Y.; Chan, S. K.; Sou, I. K.; Chan, Y. F.; Su, D. S.; Wang, N. *Adv. Mater.* **2006**, *18*, 109.

[21] Park, W. I.; Zheng, G.; Jiang, X.; Tian, B.; Lieber, C. M. *Nano Lett.* **2008**, *8*, 3004.

[22] Ma, D. D. D.; Lee, C. S.; Au, F. C. K.; Tong, S. Y.; Lee, S. T. *Science* **2003**, *299*, 1874.

[23] Boland, J. J. *Phys. Rev. Lett.* **1990**, *65*, 3325.

[24] Lin, M. C.; Chu, C. J.; Tsai, L. C.; Lin, H. Y.; Wu, C. S.; Wu, Y. P.; Wu, Y. N.; Shieh, D. B.; Su, Y. W.; Chen, C. D. *Nano Lett.* **2007**, *7*, 3656.

[25] Henderson, M. *Surf. Sci. Rep.* **2002**, *46*, 1.

[26] Lee, S. S.; Baik, J. Y.; An, K. S.; Suh, Y. D.; Oh, J. H.; Kim, Y. *J. Phys. Chem. B* **2004**, *108*, 15128.

[27] Xu, X. and Servati, P. *Nano Lett.* **2009**, *9*, 1999.

[28] Huang, Y.; Duan, X.; Cui, Y.; Lieber, C. M. *Nano Lett.* **2002**, *2*, 101.

[29] Duan, X.; Huang, Y.; Cui, Y.; Wang, J.; Lieber, C. M. *Nature (London)* **2001**, *409*, 66.

[30] Cui, Y.; Duan, X.; Hu, J.; Lieber, C. M. *J. Phys. Chem. B* **2000**, *104*, 5213.

[31] Hanrath, T.; Korgel, B. A. *J. Am. Chem. Soc.* **2004**, *126*, 15466.

[32] He, J. L.; Lu, Z. H.; Mitchell, S. A.; Wayner, D. D. M. *J. Am. Chem. Soc.* **1998**, *120*, 2660.

[33] Wang, D.; Chang, Y.;, Liu, Z.; Dai, H. *J. Am. Chem. Soc.* **2005**, *127*, 11871.

[34] Greytak, A. B.; Lauhon, L. J.; Gudiksen, M. S.; Lieber, C. M. *Appl. Phys. Lett.* **2004**, *84*, 4176.

[35] Lin, H. C.; Su, C. J.; Hsiao, C. Y.; Yang, Y. S.; Huang, T. Y. *Appl. Phys. Lett.* **2007**, *91*, 202113.

[36] Lin, C. H.; Hsiao, C. Y.; Hung, C. H.; Lo, Y. R.; Lee, C. C.; Su, C. J.; Lin, H. C.; Ko, F. H.; Huang, T. Y.; Yang, Y. S. *Chem. Commun.* **2008**, 5749.

[37] Tian, B.; Zheng, X.; Kempa, T. J.; Fang, Y.; Yu, N.; Yu, G.; Huang, J.; Lieber, C. M. *Nature (London)* **2007**, *449*, 885.

[38] Law, M.; Greene, L. E.; Johnson, J. C.; Saykally, R.; Yang, P. *Nature Mater.* **2005**, *4*, 455.

[39] Aberle, A. G. *Prog. Photovolt. Res. Appl.* **2000**, *8*, 473.

[40] Vo, T.; Williamson, A. J.; Galli, G. *Phys. ReV. B* **2006**, *74*, 045116.

[41] Zhang, R. Q.; Lifshitz, Y.; Ma, D. D. D.; Zhao, Y. L.; Frauenheim, T.; Lee, S. T.; Tong, S. Y. *J. Chem. Phys.* **2005**, *123*, 144703.

[42] Ordejón, P.; Artacho, E.; Soler, J. M. *Phys. Rev. B* **1996**, *53*, R10441.

[43] Hamann, D. R.; Schluter, M.; Chiang, C. *Phys. Rev. Lett.* **1979**, *43*, 1494.

[44] Bachelet, G. B.; Hamann, D. R.; Schluter, M. *Phys. Rev. B* **1982**, *26*, 4199.

[45] Kleinman, L.; Bylander, D. M. *Phys. Rev. Lett.* **1982**, *48*, 1425.

[46] Perdew, J. P.; Zunger, A. *Phys. Rev. B* **1981**, *23*, 5048. Phys Rev B 23:5048

[47] Perdew, J. P.; Burke, K.; Ernzerhof, M. *Phys. Rev. Lett.* **1996**, *77*, 3865.

[48] Hybertsen, M. S.; Louie, S. G. *Phys. Rev. B* **1986**, *34*, 5390.

[49] Onida, G.; Reining, L.; Godby, R. W.; Del Sole, R.; Andreoni, W. *Phys. Rev. Lett.* **1995**, *75*, 818.

[50] Yan, J. A.; Yang, L.; Chou, M. Y. *Phys. ReV. B* **2007**, *76*, 115319.

Chapter 2

Facet-dependent Electronic Properties of Hexagonal Silicon Nanowires under Progressive Hydroxylation and Surface Reconstruction

2.1 Introduction

Silicon nanowires (SiNWs) have become promising for electronic applications such as transistors [1], photovoltaic devices [2], thermoelectric power generation, and biosensors [3] due to their properties such as large surface-to-volume ratio (SVR), high carrier transport mobility, and tunable band structure not present in the bulk. As quasi-one-dimensional material systems, SiNWs exhibit unique electronic and optical properties due to quantum confinement effects arising from their nanoscale cross section. For example, a direct gap is calculated for [110] NWs with hexagonal cross section with a diameter of up to 7 nm [4], a phenomena that is promising for use of SiNWs in optoelectronic applications. While these properties are mainly determined by the diameter, crystallinity, and orientation of the NW core, they can be drastically influenced by surface properties including surface defects

A version of this chapter has been published. Xu, X. and Servati, P. (2009) Facet-dependent Electronic Properties of Hexagonal Silicon Nanowires under Progressive Hydroxylation and Surface Reconstruction. Nano Letters. 9:1999-2004.

and surface termination bonds. Generally, the surfaces of Si NWs and nanocrystals are modified to control and reduce surface dangling bonds that can introduce electronic levels inside the band gap. For example, Tian *et al.* [2] have shown that the open circuit voltage and efficiency of SiNW photovoltaic devices can be enhanced by proper passivation of NW surface and grain boundaries due to suppression of recombination processes. In addition, dramatic improvements in carrier mobility, threshold voltage, and stability of poly-Si NW devices used in wet ambient conditions are primarily attributed to H^+ and/or OH^- surface passivation effects [5].

Most of the theoretical calculations to date have been done to study the influences of crystalline orientations and the diameters on the electronic properties of SiNWs using ab initio density functional theory (DFT) [6–10]. These DFT calculations have reliably predicted that as the diameter of silicon NWs and nanocrystals are reduced, quantum confinement leads to a general increase in the band gap. More specifically, the band gap of SiNWs is shown to linearly scale with SVR for different NW cross sections [4]. On the other hand, it has been shown that the interaction of the surface termination groups with the valence band edge competes against the quantum confinement effects and can induce a reduction in the band gap [11]. Recent theoretical studies on surface passivation focused on the effect of different types of chemicals and their surface coverage on electronic structure of SiNWs [6, 11, 12]. The effect of surface termination groups on electronic structure can change for different facets of SiNW, and the role of different facets in tuning the electronic properties is not clear yet. Recently, it was shown that bonding of radical NH_2 to the different facets can have different contributions to the density of states, which helps in choosing the right facets for making SiNW sensors [13].

In this paper, we use state-of-the-art first principles calculations to investigate the effect of progressive hydroxylation on (111) and (001) SiNW facets and how the electronic properties are affected by the facet morphologies. Hydroxyl groups on the surface are important models for technologically relevant processes including oxidized SiNW surfaces and can be used to prepare an ideal surface for atomic layer deposition of metal oxide dielectrics, based on ligand exchange reaction. Many theoretical studies on hydroxylation of silicon nanocrystals have been reported in the past years [14, 15]. Here, we consider small diameter [110] SiNWs that are shown to be preferred due to development of lower energy surfaces such as (111) and (001). We also explore surface reconstruction in (001) planes. The

sensitivity of different facets to hydroxylation is shown to be dependent on the presence of surface reconstruction.

2.2 Methodology

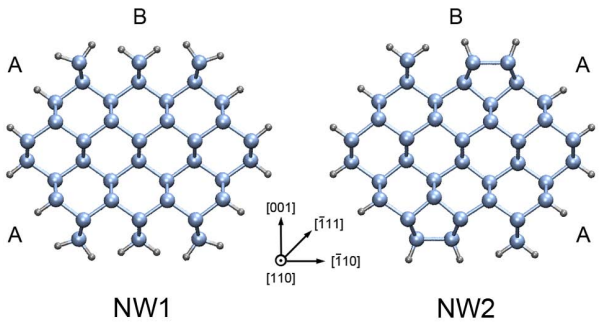

Figure 2.1: The cross section of the two types of SiNWs studied here after relaxation. The left structure is referred to as NW1 and the other NW2 with surface reconstruction as described in the text. NWs are oriented along [110]. Suffixes A and B denote (111)-type and (001)-type facets, respectively. The cyan balls represent Si atoms and the gray denotes H atoms.

The SiNW structures have been constructed along the [110] direction with hexagonal cross section and diameters of about 1.7 nm which have been observed experimentally [16, 17]. Reference [18] has predicted that hexagonal wires become stable starting at about 1.2 nm diameter which is close to a recent reported experimental value of about 3 nm [18]. Each nanowire contains four (111)-type facets and two (001)- type facets which are the low-free-energy planes for $\langle 110 \rangle$ growth axis [16]. On the (111)-type facets, each Si atom is bonded to a single H atom. For the (001) facets, two surface structures were considered in order to study the effects of (001) surface reconstruction. The first type is the symmetric SiH_2 dihydrides structure (labeled NW1) where two H atoms are bonded to one Si atom (Figure 2.1). The other type (denoted as NW2) involves surface reconstruction (Figure 2.1) on the (001) facets where a pair of H atoms on each (001) facet are removed and an additional Si-Si bond is formed. This modification is referred to as a (2×1) surface reconstruction which is well studied for bulk Si(001) surfaces. Since there is one dihydride

left on each (001) facet, the reconstructed (001) surfaces become a (3 × 1) structure which has been observed for bulk silicon (001) surface by scanning tunneling microscopy (STM) [19, 20]. For both surface structures, we first study the NW with full H-passivation, followed by gradual introduction of hydroxyl (-OH) on (001) or (111) facets. We use suffix A to denote OH-passivation on (111)-type facets and use suffix B for OH passivation on (001)-type facets. For example, NW2A-4OH is the NW with surface reconstruction where four H bonds on (111) facets of one unit cell are replaced by OH. The calculations in this work have been performed in the framework of ab initio DFT [21] within the local density approximation (LDA) [22]. We have used a double-ζ polarized basis [23] set with pseudopotential constructed using a Troullier-Martins scheme [24]. The structural relaxation was performed using conjugated gradient minimization such that the force on each atom is less than 0.04 eV/$\mathring{A}$. The distance between the NW and its images was about 18 $\mathring{A}$ which is enough to avoid any interactions between the NW images. The cutoff for the grid integration was taken to be 200 eV. The Brillouin zone was sampled by up to five Monkhorst-Pack k-points along the nanowire axis. To calculate the electronic density of states (DOS), the Brillouin zone sampling was increased to 11 k-points.

2.3 Results and discussions

Figure 2.1 shows a schematic of SiNW after relaxation, demonstrating a bulklike configuration due to the H-passivation layer. Due to the strong interaction between the adjacent dihydrides on the (001) facets of the NW1 category, the dihydrides repel each other and slightly rotate toward the (111) facets in the relaxed structure as shown in Figure 2.1. In the relaxed structure of NW2, the single dihydride on (001) facet does not rotate because of the (3 × 1) reconstruction on the surface. We also found that the O-H bonds on the (001) facets will be different from that on the (111) facets. Figure 2.2 shows two hydroxyl groups bonding to a single Si atom on the (001) facet of NW1B-4OH. Both cis and trans structures can be observed on the (001) facets with no reconstruction, while the hydroxyl groups on the (111) facets are symmetric and located in the cross-section plane of the NW. In contrast, in the NW2 category because of the larger H-H separation on the (001) facets, hydroxyl groups are in the same cross-sectional plane of the NW.

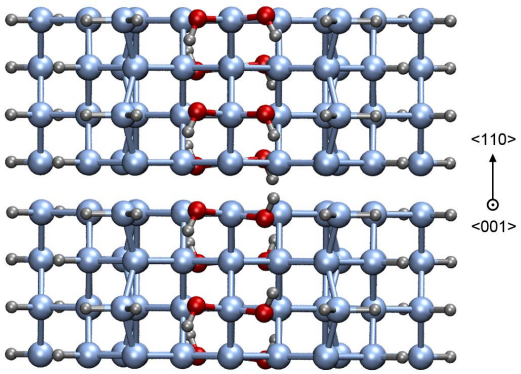

Figure 2.2: Cis (top) and trans structures (bottom) of hydroxyl groups on the (001) facets of NW1B-4OH after structural relaxation. The cyan, red, and gray balls represent the Si, O, and H atoms, respectively.

The formation energy of the NW system can be calculated by [7]

$$E_{form} = E_{tot}(wire) - \sum_{i=Si,O,H}^{\infty} N_i \mu_i \tag{2.1}$$

where E_{tot} is the total energy of the nanowire, i represents different species, and μ_i is the corresponding chemical potential of the species. The chemical potential of silicon is taken as that of bulk silicon, and the chemical potential of hydrogen and oxygen are extracted from molecular hydrogen and oxygen, respectively. The formation energy analysis (see Table 2.1) shows that the H-passivated NWs are metastable as indicated by their positive formation energies [25]. The surface-reconstructed structure (NW2) is more stable than NW1 with an energy difference of 0.678 eV due to a larger separation of hydrogen atoms on the surfaces. We can also see that both NW structures show a monotonically decreasing formation energy as the number of OH radicals increase, implying that hydroxylation is an energetically favorable process. Interestingly, we found that for the same number of OH groups, hydroxylation on (001)-type facets results in lower energy than that on (111)-type facets. This can be clearly observed from the formation energies of NW1A-4OH and NW1B-4OH. This is also the case for surfacereconstructed NW that shows hydroxylation on (001)-type facets is more energetically stable (see NW2B-4OH and NW2A-4OH).

Table 2.1: Calculated Formation Energies, Band Energies for All Systems[a]

system	E_{form} (eV)	CB (eV)	VB (eV)	ΔE_g (%)
NW1	5.512	-3.819	-5.142	
NW1A-2OH	-25.038	-3.827	-5.094	-4.23
NW1A-4OH	-55.578	-3.870	-5.064	-9.76
NW1B-2OH	-25.447	-3.809	-5.101	-2.37
NW1B-4OH	-57.708	-3.807	-5.077	-4.15
NW2	4.834	-3.856	-5.156	
NW2A-2OH	-25.732	-3.878	-5.113	-5.03
NW2A-4OH	-56.356	-3.955	-5.104	-11.58
NW2B-2OH	-25.866	-3.983	-5.105	-13.69
NW2B-4OH	-57.436	-3.788	-4.813	-21.18

[a] ΔE_g (in percentage) is the change in the energy gap compared to the original systems (NW1 or NW2) with full hydrogen passivation.

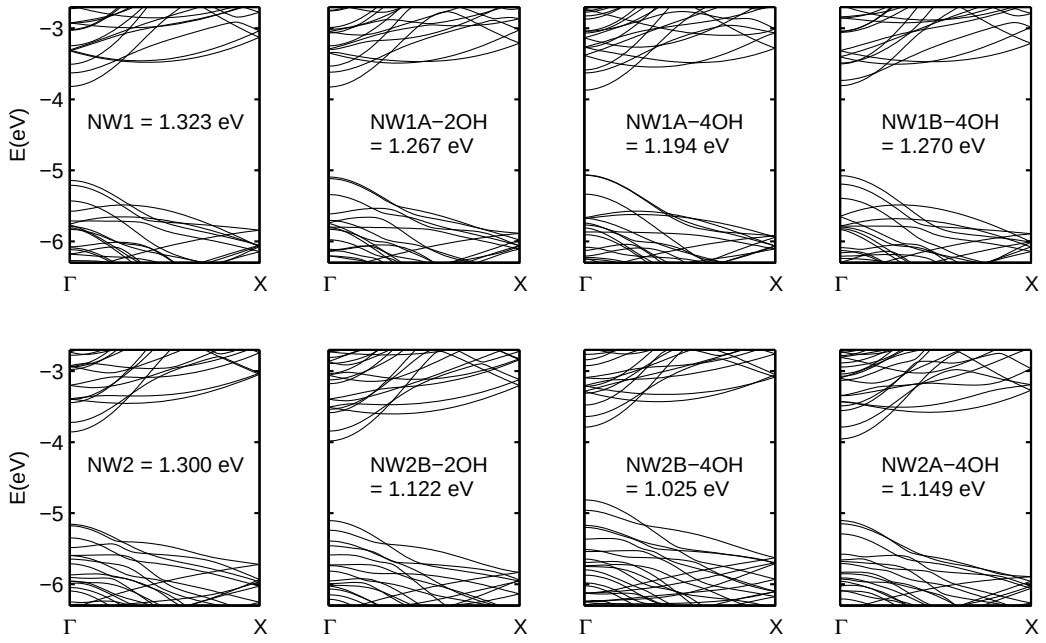

Figure 2.3: Electronic band structures and band gap of different SiNWs. The Fermi levels are all in the middle of the band gaps. k-points are sampled along $\Gamma - X$.

Table 2.2: The Changes in the Electronic Band Gap (E_g) Due to (001) Surface Reconstruction for NWs with Different Diameters[a]

D (nm)	E_g (eV)	$E_g{}'$ (eV)	ΔE_g (%)
1.4	1.402	1.356	-3.28
1.7[b]	1.323	1.300	-1.74
2.6	1.102	1.128	2.36

[a] $E_g{}'$ is the corresponding band gap after surface reconstruction; ΔE_g (in percentage) is the change in the energy gap compared to the structure before surface reconstruction. [b] The NW with diameter 1.7 nm corresponds to NW1 shown in Figure 2.1.

In this report, a direct band gap is seen (Figure 2.3) in all calculations, as the valence band peak and the minimum of the conduction band are at the Γ points. The band gaps we obtained for NW1 (1.3231 eV) and NW2 (1.3002 eV) are similar to the results of the hydrogenated SiNWs reported in ref [9]. The lowest band gap is found in NW2B-4OH which is 1.0248 eV. As discussed in ref [11], although LDA-DFT calculations underestimate the band gap of [110] nanowires, the trends in the band gap can still be predicted correctly [26, 27]. Comparing the band gap of the NW1 group and that of the NW2 group, we can see that (001) surface reconstruction induces a red shift in the band gap, which has been observed experimentally in silicon nanoparticles [15, 28, 29]. However, ref [12] showed that (001) surface reconstruction leads to a larger band gap due to the slight reduction in effective size. To further investigate the surface reconstruction effect on the band gap, we calculated the change in band gap for two SiNWs with hexagonal cross section but different diameters and surface-to-volume ratios. As shown in Table 2.2, for the SiNW with diameter about 2.6 nm, the change in the band gap due to surface reconstruction is 2.36% larger. In contrast, for the SiNW with diameter of about 1.4 nm (*i.e.*, smaller than our current NW), a stronger red shift is observed: the band gap is reduced by 3.28% after surface reconstruction. On the basis of these results, we conclude that the impact of surface reconstruction on the band gap is size-dependent, which explains the discrepancy with ref [12].

Generally, hydroxylation reduces the energy gap in comparison to H-passivation. As shown in Figure 2.3, the change in the maximum energy of the valence band is more significant as compared to the change in the minimum of the conduction band. For NW1A-2OH, NW1A-

Table 2.3: Calculated Ratios of Effective Masses for Electron ($m_e{}^*$) and Hole ($m_h{}^*$) to the Mass of a Free Electron m for All Systems

system	$m_e{}^*/m$	$m_h{}^*/m$
NW1	0.1260	0.1614
NW1A-2OH	0.1265	0.1649
NW1A-4OH	0.1270	0.1656
NW1B-2OH	0.1244	0.1584
NW1B-4OH	0.1247	0.1545
NW2	0.1191	0.1785
NW2A-2OH	0.1194	0.1703
NW2A-4OH	0.1203	0.1560
NW2B-2OH	0.1186	0.1613
NW2B-4OH	0.1197	0.1634

4OH, and NW2, the second valence band maximum is located just below the first one. Comparing NW1, NW1A-2OH, and NW1A-4OH, it can be observed that the reduction in the band gap values becomes more noticeable as the surface coverage of OH increases. The band gap of NW1A-2OH is reduced by 4.23%, while for NW1A-4OH it is reduced by 9.76%. However, the effect of OH passivation on (001)-type facets is different from that on (111)-type facets. Since NW1A-4OH and NW1B-4OH have the same number of atoms, we can compare them directly with NW1. The energy gap is only reduced by 4.15% with four OH bonded on the (001) facets, while the passivation on (111) facets with the same amount of OH shrinks the energy gap by 9.76%, which is more than twice larger. In contrast, the same analysis on NW2 shows that the reconstructed (001) facets seem to be more active in band gap modification. The band gap of NW2B-4OH is reduced by 21.18% with respect to NW2. These results go to show that the effect of hydroxylation is strongly facet dependent, which is very important for design and implementation of NW based biological and chemical sensors due to the fact that the density of carriers in NWs changes exponentially with a change in the band gap.

Table 2.3 summarizes the corresponding effective masses for different NWs. The effective masses of holes and electrons are determined directly from the curvatures of the valence and the conduction bands, respectively. The calculated effective masses of NW1 and NW2 which are passivated only with hydrogen agree well with the results reported in ref [30]. As

expected, the changes in electronic band structure lead to changes in the effective masses. It is found that for both NW1 and NW2 groups the effective mass of electron increases slightly as OH is introduced to the (111)- type facets (NW1A and NW2A in Table 2.3). In contrast, hydroxylation on (001) facets decreases effective masses for both electrons and holes. However, this trend in the change of effective masses is not observed in the SiNWs with surface reconstruction (NW2 category in Table 2.3). Our results show that the effective masses of electrons in NW2 category are generally smaller than that of NW1, while the effective masses of holes are larger as compared to the NW1 group.

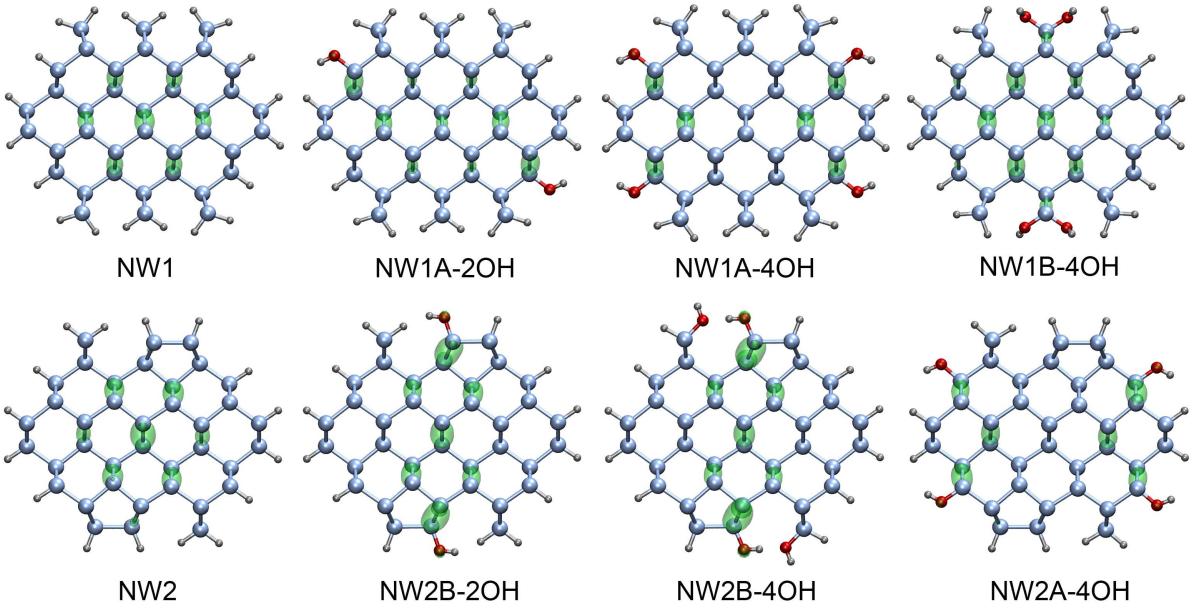

Figure 2.4: HOMO orbital wave functions (of the same contour value 0.045) associated with different NW systems. The cyan, red, and gray balls represent the Si, O, and H atoms, respectively.

After the structures were fully relaxed by the DFT-LDA approach, the molecular orbitals were calculated at the B3LYP/6-31G(d) [31] level of theory using the Gaussian 03 package [32]. It is found that the presence of hydroxyl groups on the NW surfaces delocalizes the highest occupied molecular orbitals (HOMO), while the lowest unoccupied molecular orbitals (LUMO) remain highly localized at the center of the NW (not shown here). Figure 2.4 shows the HOMO of NW1 and NW2 with and without hydroxylation. The charge

distributions are generally around the Si-Si bonds along the nanowire's axis. When the NW is fully passivated with hydrogen, the HOMO is concentrated more in the interior of the NW. As OH passivation increases on the (111)-type facets of both types of NWs, the HOMO densities spread out to the surface and mostly toward the hydroxyl groups. However, hydroxylation on the (001) facets shows different results for NW1 and NW2. While for NW1 hydroxylation does not change the HOMO significantly, for NW2 the hydroxyl groups displace the HOMO states toward the surface. In NW1B-4OH, a large contribution around the center of NW remains and the induced surface states are small. Note that the nonsymmetric nature of HOMO densities for NW1B-4OH is due to the cis and trans structures on two (001) facets. In NW2B-2OH/4OH, although the interior orbital remains, there is a significant contribution from the passivation sites as well on the reconstructed surfaces. The difference must be due to the different surface structure of the (001) facets. We can conclude that the common effect observed in both NW1 and NW2 categories due to surface modification is that hydroxylation on (001) facets does not change the HOMO around the center of the wire, while OH-passivation on (111) facets can significantly shift the HOMO from the center to a close proximity of the passivation sites. This can explain the change in the electronic band structures. The surface states induced by OH passivation cause significant changes in the valence band maxima (VBM) at the Γ point, while the conduction band minima (CBM) are relatively stable.

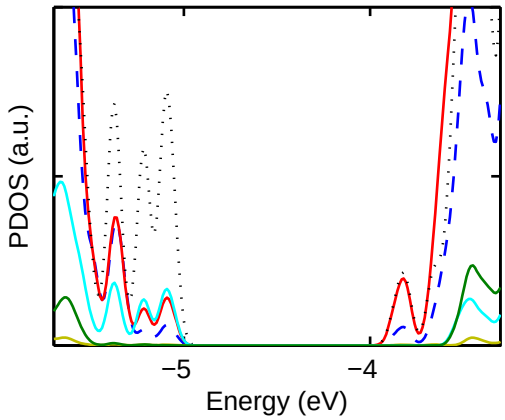

Figure 2.5: PDOS plots for H (yellow solid), O (cyan solid), and Si (black dot) atoms on (111) facets, H (green solid) and Si (blue dash) atoms on (001) facets, and Si (red solid) atoms around the center for NW1A-4OH.

In order to understand the effect of hydroxylation on the electronic band structures, we also examine the partial density of states (PDOS). The calculation of PDOS is discussed in Appendix B. The total electronic DOS was decomposed into partial atomic contributions from different species and atoms at different sites. The PDOS curves were normalized by the total number of atoms. A Gaussian broadening of 0.05 eV was used. The PDOS contributions form the terminating groups (H, O) and the two types of Si atoms (one on the surfaces and one around the center) of NW1A-4OH are displayed in Figure 2.5. As reported in ref [13], the surface states of SiNWs seem to be more relevant in the formation of the VBM states. The main contribution to the DOS near the VBM is from the Si atoms at the hydroxyl sites (in this case on (111) facets), as can be seen in Figure 2.5 by comparing the first peaks of the PDOS graphs of different atoms. The next two contributions, although at lower level, are from the O atom at the hydroxyl site and the Si atom around the center. However, the contributions from the Si atom on the facets with no hydroxyl group (*i.e.*, (001) facets in this case) and the H atoms are relatively small. Similar effects are observed in NW2A-4OH and NW2B-4OH as well.

Since we know Si atoms play an important role in the DOS, we then plot the PDOS derived from Si atoms at different sites for both NW1 and NW2 categories. The three plots in Figure 2.6 are for NW2, NW2B-4OH, and NW2A- 4OH, respectively. For NW2 with H only passivation, the contributions of the silicon atoms on (001) and (111) facets and around the wire center to the DOS near the valence band edges are very similar. For NW2B-4OH where hydroxyls are absorbed on the (001)-type facets, the contribution to the valence band edge from the Si atoms on (111) facets dominates which is about 3 times larger. When hydroxyls are absorbed on the (111)-type facets (NW2A-4OH), the Si atoms on (111) facets contribute the most. This is consistent with the fact that the HOMO densities move toward the hydroxyl sites. For the states near the CBM, the contribution from the central atoms always dominates. But there is no significant difference among the Si atoms from these three sites. Figure 2.7 shows similar PDOS analysis for NWs from the NW1 group. In contrast to the NW2 group, where both the reconstructed (001) and the monohydrated (111) facets have significant contributions to the band-edge, the monohydrated (111) facets of NW1 seems to be more active than the symmetric (001) facets. Hydroxylation on the symmetric (001) facets of NW1 does not create states close to VBM. This difference must be due to the variation in the (001) facet morphology as

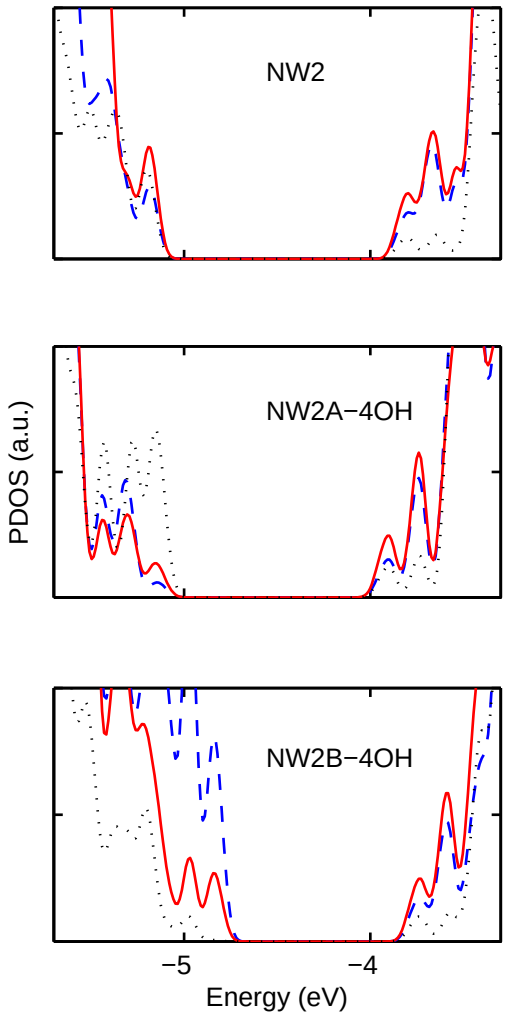

Figure 2.6: PDOS of silicon atoms on (001) surface facets (blue dash), (111) surface facets (black dot), and around the center (red solid) for NW2, NW2B-4OH, and NW2A-4OH.

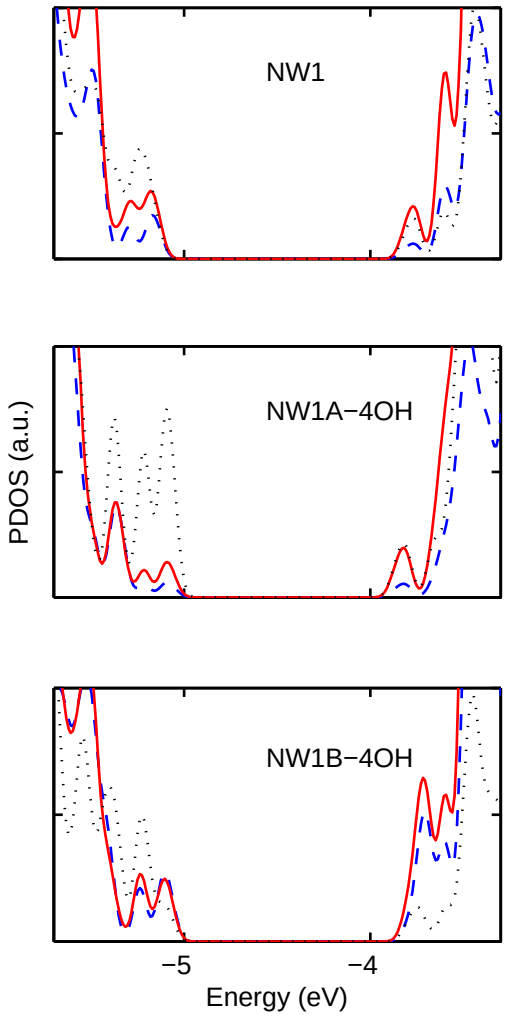

Figure 2.7: PDOS plots of silicon atoms on (001) surface facets (blue dash), (111) surface facets (black dot), and around the center (red solid) for NW1, NW1A-4OH, and NW1B-4OH.

observed in the HOMO density.

2.4 Conclusion

In conclusion, we have investigated the effect of hydroxylation and surface reconstruction on electronic properties of SiNWs including band gap, effective mass, and density of states. In contrast to confinement effects, the size of the band gap decreases by increasing the amount of hydroxyl groups on the surface. The decrease in band gap is more pronounced ($\sim$ 10%) for hydroxyl groups on (111) facets in comparison to those on (001) facets ($\sim$4%), when there is no reconstruction. But for NWs with reconstructed (001) facets, a decrease in band gap of about 21% can be observed for hydroxylation on reconstructed surfaces. A decrease in band gap of these NWs is accompanied by a general movement of charge densities arising from HOMO from the center of NW toward the surface. While effective masses for electrons and holes do not significantly change upon hydroxylation, reconstruction induces a small decrease in effective mass of electrons and a small increase in effective mass of holes. PDOS analysis for hydroxylated NWs also shows that the contributions of the surface Si atoms on either (001) or (111) facets will dominate the density of states around the VBM. The sensitivity of density of states to hydroxylation on (111) facets is pronounced for NWs with no surface reconstruction, while this is more pronounced for hydroxylation on reconstructed (001) surfaces. These results are important for understanding the effect of surface termination on the electronic properties of SiNWs and can be used for design of NW sensors and optimization of surface chemistry for SiNW transistors.

Acknowledgment

We gratefully acknowledge the financial support of the Natural Sciences and Engineering Research Council (NSERC) of Canada for this project. We also thank Dr. Alireza Nojeh for helpful discussions.

Bibliography

[1] Cui, Y.; Zhong, Z.; Wang, D.; Wang, W. U.; Lieber, C. M. *Nano Lett.* **2003**, *3*, 149. Colli, A.; Fasoli, A.; Beecher, P.; Servati, P.; Pisana, S.; Fu, Y.; Flewitt, A. J.; Milne, W. I.; Robertson, J.; Ducati, C.; De Franceschi, S.; Hofmann, S.; Ferrari, A. C. *J. Appl. Phys.* **2007**, *102*, 034302.

[2] Tian, B.; Zheng, X.; Kempa, T. J.; Fang, Y.; Yu, N.; Yu, G.; Huang, J.; Lieber, C. M. *Nature (London)* **2007**, *449*, 885.

[3] Lin, M. C.; Chu, C. J.; Tsai, L. C.; Lin, H. Y.; Wu, C. S.; Wu, T. P.; Wu, Y. N.; Shieh, D. B.; Su, Y. W.; Chen, C. D. *Nano Lett.* **2007**, *7*, 3656.

[4] Yao, D.; Zhang, G.; Li, B. *Nano Lett.* **2008**, *8*, 4557.

[5] Lin, H. C.; Su, C. J.; Hsiao, C. Y.; Yang, Y. S.; Huang, T. Y. *Appl. Phys. Lett.* **2007**, *91*, 202113. Appl.

[6] Ng, M. F.; Zhou, L.; Yang, S. W.; Sim, L. Y.; Tan, V. B. C.; Wu, P. *Phys. ReV. B* **2007**, *76*, 155435.

[7] Aradi, B.; Ramos, L. E.; Deák, P.; Köhler, Th.; Bechstedt, F.; Zhang, R. Q.; Frauenheim, Th. *Phys. ReV. B* **2007**, *76*, 035305.

[8] Vo, T.; Williamson, A. J.; Galli, G. *Phys. ReV. B* **2006**, *74*, 045116.

[9] Singh, A. K.; Kumar, V.; Note, R.; Kawazoe, Y. *Nano Lett.* **2006**, *6*, 920.

[10] Zhang, R. Q.; Lifshitz, Y.; Ma, D. D. D.; Zhao, Y. L.; Frauenheim, T.; Lee, S. T.; Tong, S. Y. *J. Chem. Phys.* **2005**, *123*, 144703.

[11] Nolan, M.; O'Callaghan, S.; Fagas, G.; Greer, J. C.; Frauenheim, T. *Nano Lett.* **2007**, *7*, 34.

[12] Leu, P. W.; Shan, B.; Cho, K. *Phys. ReV. B* **2006**, *73*, 195320.

[13] Leao, C. R.; Fazzio, A.; da Silva, A. J. R. *Nano Lett.* **2007**, *7*, 1172.

[14] Carniato, S.; Gallet, J.-J.; Rochet, F.; Dufour, G.; Bournel, F.; Rangan, S.; Verdini, A.; Floreano, L. *Phys. ReV. B* **2007**, *76*, 085321.

[15] Ramos, L. E.; Furthmüller, J.; Bechstedt, F. *Phys. Rev. B* **2004**, *70*, 033311.

[16] Wu, Y.; Cui, Y.; Huynh, L.; Barrelet, C. J.; Bell, D. C.; Lieber, C. M. *Nano Lett.* **2004**, *4*, 433.

[17] Ma, D. D. D.; Lee, C. S.; Au, F. C. K.; Tong, S. Y.; Lee, S. T. *Science* **2003**, *299*, 1874.

[18] Chan, T.-L.; Ciobanu, C. V.; Chuang, F.-C.; Lu, N.; Wang, C.-Z.; Ho, K.-M. *Nano Lett.* **2006**, *6*, 277.

[19] Boland, J. J. *Phys. Rev. Lett.* **1990**, *65*, 3325.

[20] Boland, J. J. *Surf. Sci.* **1992**, *261*, 17.

[21] Ordejón, P.; Artacho, E.; Soler, J. M. *Phys. Rev. B* **1996**, *53*, R10441.

[22] Zhao, X.; Wei, C. M.; Yang, L.; Chou, M. Y. *Phys. Rev. Lett.* **2004**, *92*, 236805.

[23] Sankey, O. F.; Niklewski, D. J. *Phys. Rev. B* **1989**, *40*, 3979.

[24] Troullier, N.; Martins, J. L. *Phys. Rev. B* **1991**, *43*, 1993.

[25] Ponomareva, I.; Menon, M.; Srivastava, D.; Andriotis, A. N. *Phys. Rev. Lett.* **2005**, *95*, 265502.

[26] Puzder, A.; Williamson, A. J.; Grossman, J. C.; Galli, G. *Phys. Rev. Lett.* **2002**, *88*, 097401.

[27] Puzder, A.; Williamson, A. J.; Grossman, J. C.; Galli, G. *J. Chem. Phys.* **2002**, *117*, 6721.

[28] Vasiliev, I.; Martin, R. M. *Phys. Status Solidi B* **2002**, *233*, 5.

[29] Puzder, A.; Williamson, A. J.; Reboredo, F. A.; Galli, G. *Phys. Rev. Lett.* **2003**, *91*, 157405.

[30] Yan, J. A.; Yang, L.; Chou, M. Y. *Phys. ReV. B* **2007**, *76*, 115319.

[31] Becke, A. D. *J. Chem. Phys.* **1993**, *98*, 5648. Stephens, P. J.; Devlin, F. J.; Chabalowski, C. F.; Frisch, M. J. *J. Phys. Chem.* **1994**, *98*, 11623.

[32] Frisch, M. J.; Trucks, G. W.; Schlegel, H. B.; Scuseria, G. E.; Robb, M. A.; Cheeseman, J. R.; Montgomery, J. A., Jr.; Vreven, T.; Kudin, K. N.; Burant, J. C.; Millam, J. M.; Iyengar, S. S.; Tomasi, J.; Barone, V.; Mennucci, B.; Cossi, M.; Scalmani, G.; Rega, N.; Petersson, G. A.; Nakatsuji, H.; Hada, M.; Ehara, M.; Toyota, K.; Fukuda, R.; Hasegawa, J.; Ishida, M.; Nakajima, T.; Honda, Y.; Kitao, O.; Nakai, H.; Klene, M.; Li, X.; Knox, J. E.; Hratchian, H. P.; Cross, J. B.; Adamo, C.; Jaramillo, J.; Gomperts, R.; Stratmann, R. E.; Yazyev, O.; Austin, A. J.; Cammi, R.; Pomelli, C.; Ochterski, J. W.; Ayala, P. Y.; Morokuma, K.; Voth, G. A.; Salvador, P.; Dannenberg, J. J.; Zakrzewski, V. G.; Dapprich, S.; Daniels, A. D.; Strain, M. C.; Farkas, O.; Malick, D. K.; Rabuck, A. D.; Raghavachari, K.; Foresman, J. B.; Ortiz, J. V.; Cui, Q.; Baboul, A. G.; Clifford, S.; Cioslowski, J.; Stefanov, B. B.; Liu, G.; Liashenko, A.; Piskorz, P.; Komaromi, I.; Martin, R. L.; Fox, D. J.; Keith, T.; Al-Laham, M. A.; Peng, C. Y.; Nanayakkara, A.; Challacombe, M.; Gill, P. M. W.; Johnson, B.; Chen, W.; Wong, M. W.; Gonzalez, C.; Pople, J. A. *Gaussian 03, Revision C.02*; Gaussian, Inc.: Wallingford, CT, 2004.

Chapter 3

Summary and Future Work

The use of nanowires is promising because of the potential applications in nanoelectronics, and also because the electronic and optical properties of nanowires can be engineered via size, material composition, and surface morphology. Theoretical study of the material properties may lead to new device applications, such as band gap engineering for device design.

Chapter 2 discussed the surface structures of SiNW and how surface modification affects its electronic properties [1]. We observed a significant change in band gap that would result via a very high change in conductance if the nanowire is used to build a sensor or a transistor. The conductance is proportional to the number of carriers and mobility. Based on the Maxwell-Boltzmann distribution, the density of carriers is proportional to exp(-E_g/2kT), which predicts an exponential change in conductance with a change in the band gap. Making a sensor or a transistor at the molecular scale requires precise control of the electronic structures. So it is expected that the change in band gap will affect the nanoelectronic device characteristics. The observation of band gap modification in SiNWs points to the possibility of new approach for designing nanoelectronic devices.

Following the work in Chapter 2, although we focused on SiNWs in this thesis, more work can be done to extend our current theoretical study to explore other interesting materials and nanowire structures. Recently, different experimental groups reported axial and radial nanowire heterostructures fabricated in a bottom-up approach [2–4]. These structures are expected to have potential applications in nanoelectronics and nano-optics. Particularly, the core-multishell structures of radial (coaxial) NW heterostructures enable new interface properties and introduce unique electronic and photonic function. For instance, the energy band line-up at the Ge and Si interface of Ge/Si core/shell NWs leads the realization

of high performance p-channel NW FETs [4]. Theoretical study of surface passivation effects will also be important for exploring the essential physics and design issues of NW heterostructure devices, since the high-sruface-area nature remains. The model used in chapter 2 can be easily transferred to a Ge/Si core/shell NW heterostructure.

In the theoretical side, researchers have recently explored strain as a method to engineer the electronic properties of SiNWs [5, 6]. They studied the effects of strain on the electronic properties of small diameter SiNWs using ab initio DFT calculations. They show that the band structures can be manipulated to have direct band gaps by applying lattice strain. Our results show that hydroxylation on NW surface shrinks the band gap and preserves the direct-gap nature, which could be easier to control during device fabrication. In addition, as shown in our calculations, the presence of hydroxyl groups on the (111)-type facets causes the HOMO states spread out to the surface while the LUMO states remain highly localized at the center of the NW. This indicates that by controlling the surface morphology of SiNW, the locations of the near-gap states (CBM and VBM) could be effectively separated and hence makes it possible to separate charges, which is valuable for the practical application of solar cells.

The preliminary investigation of gold nanoparticles deposition presented in Appendix A is an important step for studying nanowire growth, since the gold catalyst will affect the diameter, the density and the degree of epitaxy. The substrate prepared in this way will be loaded into a CVD system for subsequent nanowire growth. Other parameters such as growth temperature and gas flow rate need to be explored as well. Surface functionalization of NWs can be achieved during or after the growth process.

Bibliography

[1] Xu, X. and Servati, P. *Nano Lett.* **2009**, *9*, 1999.

[2] Lu, W.; Xiang, J.; Timko, B. P.; Wu, Y.; Lieber, C. M. *Proc. Natl. Acad. Sci. U.S.A.* **2005**, *102*, 10046.

[3] Xiang, J.; Vidan, A.; Tinkham, M.; Westervelt, R. M.; Lieber, C. M. *Nat. Nanotechnol.* **2006**, *1*, 208.

[4] Xiang, J.; Lu, W.; Hu, Y. J.; Wu, Y.; Yan, H.; Lieber, C. M. *Nature* **2006**, *441*, 489.

[5] Hong, K. H.; Kim, J.; Lee, S. H.; Shin, J. K. *Nano Lett.* **2008**, *8*, 1335.

[6] Leu, P. W.; Svizhenko, A.; Cho, K. *Phys. Rev. B* **2008**, *77*, 235305.

Appendix A

Gold Nanoparticles Deposition

As mentioned in chapter 1, a greater degree of control on the wire diameter and location can be possibly achieved by depositing gold NPs onto predefined areas. In this work, a preliminary investigation of the immobilization of citrate-stabilized gold nanoparticles on to silicon substrate was carried out using two methods. The first technique is surface modification of the substrate by amine functional group [1] and the second method is to modify the pH value of the citrate-stabilized gold colloid solution [2]. Gold nanoparticle colloids, 3-aminopropyltriethoxysilane (APTES) and 3-aminopropyltrimethoxysilane (APTMS) were obtained commercially from Sigma-Aldrich Co. And the mean diameters of NPs used in this work were 10 nm and 20 nm. The morphologies of the Au-coated surface were evaluated using AFM and SEM. The material composition was analyzed by Auger electron spectroscopy (AES).

A.1 Surface modification of Si substrate

Because citrate-stabilized gold colloids do not adhere to silicon substrate, a positively charged polyelectrolyte layer on the substrate is commonly used as a linker to attract and bind the negatively charged gold colloids. APTES is commonly used in attaching metal NPs to silica substrates because of the strong interaction between the amine group and the metal particles [3, 4]. The polymer is positively charged in aqueous solution at neutral PH and hence absorbs onto the substrate due to its electrostatic attraction to deprotonated hydroxyl groups on the silica layer. Consequently the polymer film presents a positively charged surface to the negatively charged gold colloids in aqueous solution, attracting them to the surface. When the APTES-modified surface is immersed into the

gold colloidal solution, the terminal amino groups are protonated ($-NH_2 \rightarrow -NH_3^+$). The basic mechanism of the reaction is illustrated in Figure A.1.

Figure A.1: Negatively charged citrate-stabilized gold nanoparticles are attached on the modified substrate by electrostatic interaction with the protonated amino functionality. The Au NP is acutally larger and covers several NH_3^+ groups.

The Si(100) wafers were cut into approximately 1.5 cm $\times$ 0.75 cm pieces, and cleaned in freshly made piranha solution (5:1 sulfuric acid to hydrogen peroxide) at 100 °C for 15 min. Wafers were thoroughly rinsed in DI water. After this pretreatment, the Si surface was rich in hydroxyl groups. Then, the Si slices were immersed in 10mL 2.5 mM APTES solution at room temperature for 10 min. Since APTES is very air sensitive, the diluted solution was prepared by using a syringe to extract 6μL APTES from its bottle and injecting the APTES into DI water, beneath the surface of the water. Any unreacted silane molecules were removed by further washing with DI water to avoid colloidal gold particles aggregating during the deposition process. Next, the substrate covered by a APTES monolayer were dipped into the diluted gold colloid solution (1:2 water to solution) for 30 min. The Au-coated substrates were removed, gently rinsed in DI water and finally gently blown dry with N_2. The Au NPs were not removed but were strongly immobilized on the Si substrate because of the affinity of the amino group to the gold [5] in despite of water rinsing and blown dry.

AFM tapping mode scans are presented in Figure A.2 and Figure A.3. Initially AFM images of 25 μm $\times$ 25 μm were taken to investigate the large scale coverage of the substrate. Higher resolution images of approximately 3 μm $\times$ 3 μm were also taken for detail analysis. It

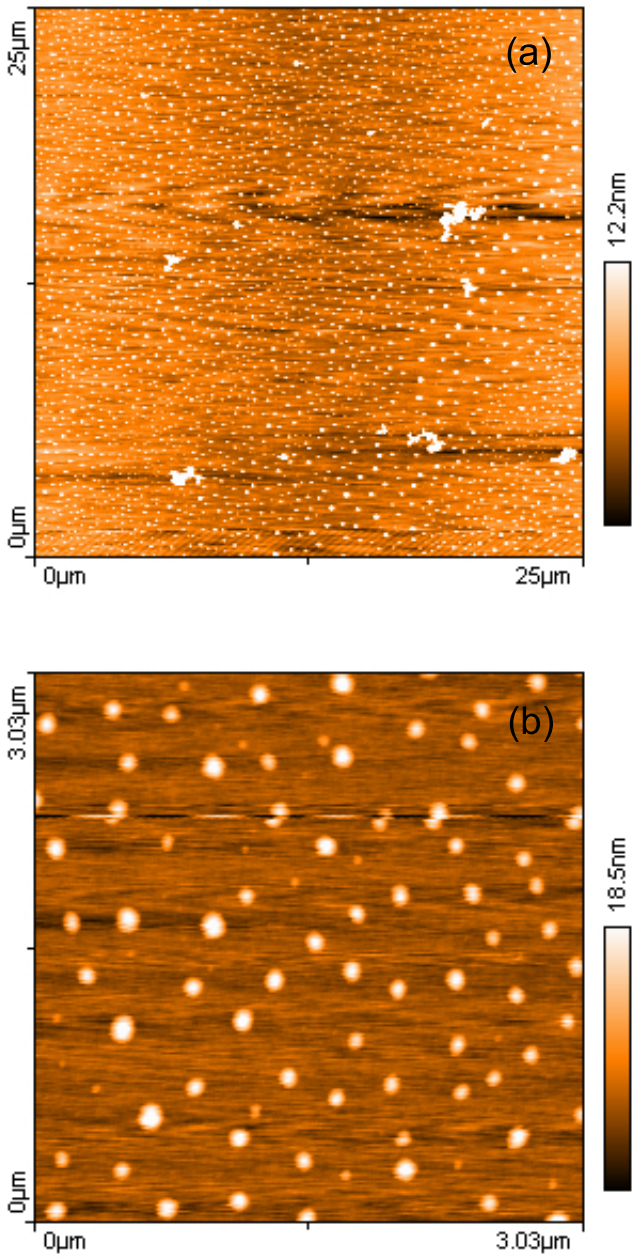

Figure A.2: Tapping mode AFM images of APTES-modified Si surface immersed in diluted citrate-stabilized gold nanoparticle (20 nm) solution (1:2 water to solution) for 30 min. The bottom figure is a higher resolution AFM image collected from the top image. The tip-sample convolution, which leads to laterally enlarged sample size, is clearly observed.

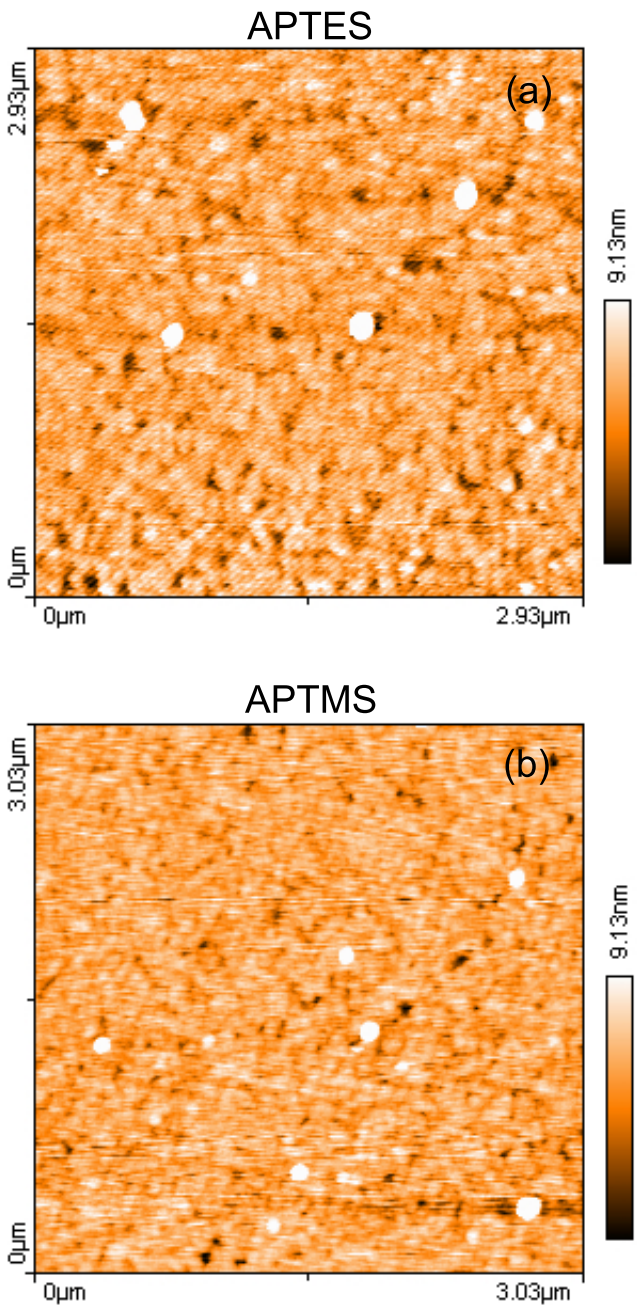

Figure A.3: Tapping mode AFM images of APTES-modified (top) and APTMS-modified (bottom) Si surfaces immersed in diluted citrate-stabilized gold nanoparticle (10 nm) solution (1:2 water to solution) for 30 min.

can be noted that the lateral dimensions of the NPs in the AFM images are considerably larger than the NP size which was determined by the vendor. This deviation is attributed to the convolution effect of the NP samples with the AFM tip [6, 7]. However, we can use the height information to derive the size of the NP. The NP height indicated in the AFM images is in good agreement with the NP size (18.5 nm $\approx$ 20 nm and 9.13 nm $\approx$ 10 nm). High magnification AFM image reveals a minor amount of smaller Au NPs distributed between the large NPs. It can also be observed from the AFM images (Figure A.2(a)) that the gold NPs in some regions appear to aggregate, *i.e.* to form larger gold nanoclusters. The observed aggregation behavior is possibly caused by the nonuniform amino silane layer on the silicon surface.

Figure A.3(a) and A.3(b) show that APTES and APTMS treatments resulted in similar gold-coated surfaces. Comparing Figure A.3 and Figure A.2(b), it seems that the 20 nm gold NPs have a greater propensity to self-organize more readily to surfaces than the 10 nm gold nanoparticles. This may be due to the larger contact areas of the 20 nm gold NPs hence stronger surface adsorption.

A.2 pH modification of Au colloid solution

Modifying silicon substrate with amino silane group provides an effective and reliable approach for controlled assembly of gold nanoparticles over coverage and the spacial distribution. However, it has been found that this deposition method prevents NW epitaxial growth on silicon substrates due to a thin oxide film formed on the silicon substrate during gold colloid deposition [2, 8]. To overcome this limitation, several groups have used high-temperature methods above 400 °C to achieve NW epitaxial growth [9, 10]. An alternative method was reported to deposit Au colloid NPs on silicon substrates without the use of polyelectrolyte layers [2]. The negative charge of the citrate ions coated on the Au NP surface may prevent gold depostion onto silicon surface. By acidifying the colloid solution, the colloids appear to be neutralized and tend to deposit. We would also like to emphasize that low-temperature (below 400 °C) epitaxial growth of GeNW was acheived by using APTES as the polyelectrolyte layer and a two-temperature growth procedure [1].

In this process, all the substrates were cleaned by HF etching then followed by RCA-1, RCA-2 cleaning in order to remove all metal contaminant and native oxide and finally with a HF-dip for 2 min. The clean silicon surface was terminated by hydrogen after these cleaning procedures. 49% HF was added to the Au colloid solution for a concentration of 0.1 M HF which lowered the pH value to 2 approximately as indicated by the pH paper. Then the gold-colloid was deposited for 2 min by dip coating.

Figure A.4 are the SEM images showing gold-colloid deposition from 2 minute exposure of hydrogen-terminated Si(100) to 10 nm gold colloid solution containing 0.1M HF. Auger electron spectroscopy (AES) analysis was also performed to characterize the surface compositions of the Au NP-modified film on the silicon wafer depicted in SEM figure. Figure A.5 reveals that when the electron beam was focused on the Au NP region (Figure A.4(b)), the Au signal can be observed through the peaks between 2000 and 2200 eV. The Au peaks are relatively small due to the small quantity of the Au particle. Beyond the NP region, *i.e.* the Si wafer background, there was no Au signal detected. Similar spectra were obtained from several other particles. From the AES data and the SEM images above we can confirm that the addition of HF to the Au colloid solution resulted in Au NPs deposition.

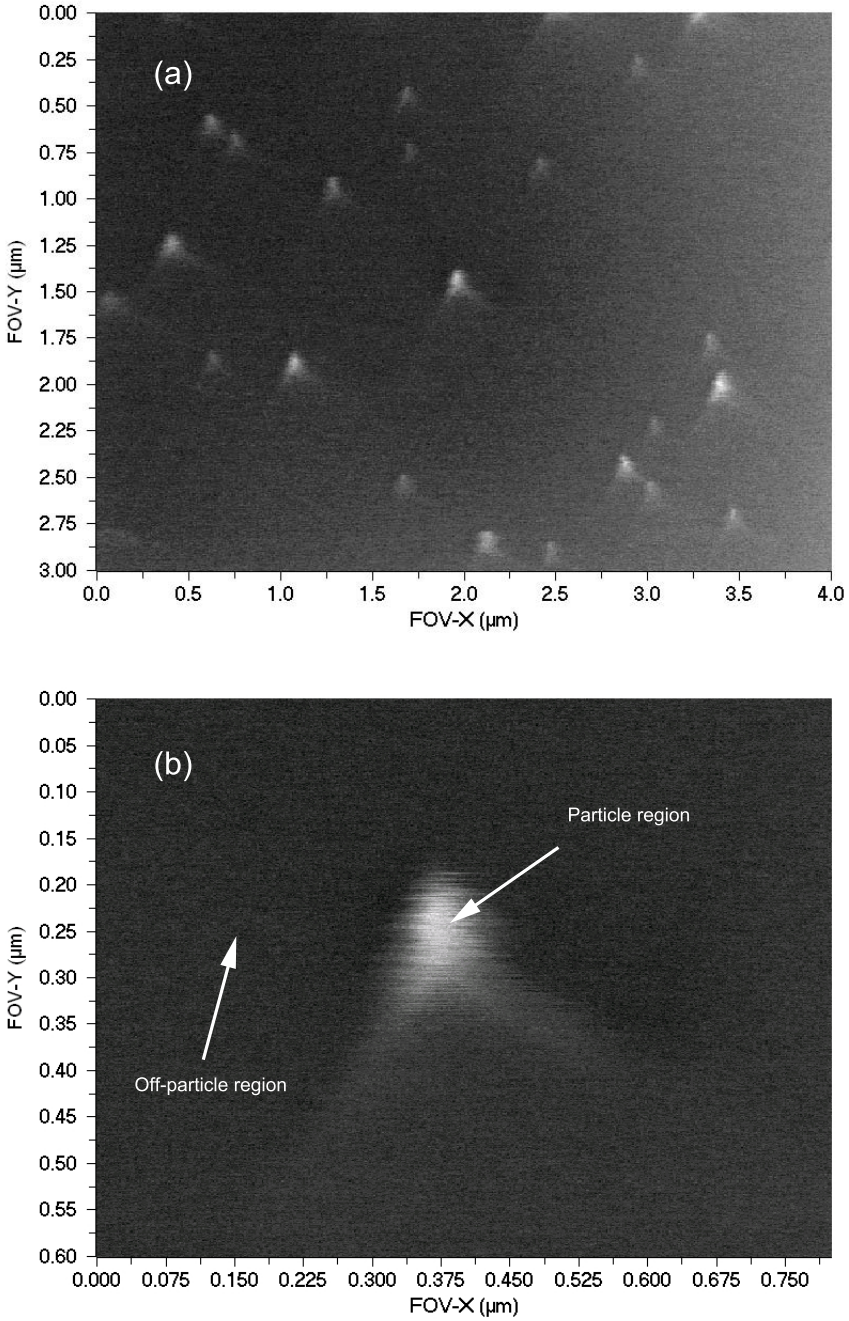

Figure A.4: SEM images of Au NP-deposited surface.

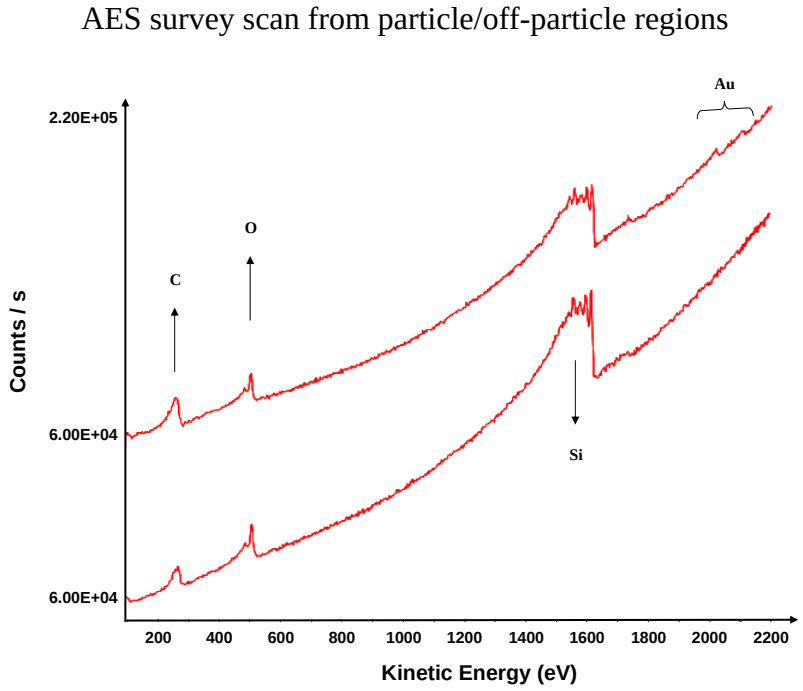

Figure A.5: AES data recorded at the particle region (top) and off-particle region (bottom) as indicated in the SEM image. The curves are offset vertically for clarity.

Bibliography

[1] Adhikari, H.; Marshall, A. F.; Chidsey, C. E. D.; and, McIntyre, P. C. *Nano Lett.* **2006**, *6*, 318.

[2] Woodruff, J. H.; Ratchford, J. B.; Goldthorpe, I. A.; McIntyre, P. C.; Chidsey, C. E. D. *Nano Lett.* **2007**, *7*, 1637.

[3] Kooij, E. S.; Brouwer, E. A. M.; Wormeester, H.; Poelsema, B. *Langmuir* **2002**, *18*, 7677.

[4] Enders, D.; Nagao, T.; Pucci, A.; Nakayama, T. *Surf. Sci.* **2006**, *600*, L71.

[5] Okamoto, T.; Yamaguchi, I.; Kobayashi, T. *Optics Lett.* **2000**, *25*, 372.

[6] Wang, J.; Zhu, T.; Song, J.;Liu, Z. *Thin Solid Films* **1998**, *591*, 327.

[7] Keller, D. *Surf. Sci.* **1991**, *253*, 353.

[8] Cui, Y.; Lauhon, L. J.; Gudiksen, M. S.; Wang, J. F.; Lieber, C. M. *Appl. Phys. Lett.* **2001**, *78*, 2214.

[9] Kamins, T. I.; Li, X.; Williams, R. S. *Nano Lett.* **2004**, *4*, 503.

[10] Hochbaum, A. I., Fan, R.; He, R.; Yang, P. *Nano Lett.* **2005**, *5*, 457.

Appendix B

Partial Density of States in SIESTA

In SIESTA, the density of states (DOS) is calculated by

$$g(E) = \frac{1}{N_{\vec{k}}} \sum_{i}^{bands} \sum_{\vec{k}} \delta(E - E_i(\vec{k})) \tag{B.1}$$

And the partial density of states (PDOS) with weight on orbital μ is defined as

$$g_\mu(E) = \frac{1}{N_{\vec{k}}} \sum_{i}^{bands} \sum_{\vec{k}} \sum_{\nu} C^*_{\nu i}(\vec{k}) C_{\mu i}(\vec{k}) S_{\nu\mu}(\vec{k}) \delta(E - E_i(\vec{k})) \tag{B.2}$$

Where the $C_{\nu i}$ and $C_{\mu i}$ are the coefficients of the eigenvector $\psi_i(\vec{k})$ with eigenvalue $E_i(\vec{k})$; and $S_{\nu\mu}$ is the overlap matrix of the atomic orbital ϕ_ν and ϕ_μ.

The sum of PDOS over all orbitals gives the total DOS:

$$g(E) = \sum_{\mu} g_\mu(E) \tag{B.3}$$

Then, a gaussian function is used to broaden the eigenvalues and smooth the shapes of the

DOS and PDOS:

$$\delta(E - E_i(\vec{k})) \longrightarrow \frac{1}{\sigma\sqrt{\pi}} exp\left\{-\frac{(E - E_i(\vec{k}))^2}{\sigma^2}\right\} \tag{B.4}$$